

Spontaneous cold-to-hot heat transfer in Knudsen gas

Yu Qiao^{1,2,*}, Zhaoru Shang¹

¹ Program of Materials Science and Engineering, University of California – San Diego, La Jolla, CA 92093, U.S.A.

² Department of Structural Engineering, University of California – San Diego, La Jolla, CA 92093-0085, U.S.A.

* Corresponding author (email: yqiao@ucsd.edu)

Abstract: It is well known that, when in a thermal bath, a Knudsen gas may reach a nonequilibrium steady state; often, this is not treated as a thermodynamic problem. Here, we show that if incorporated in a large-sized setup, such a phenomenon has nontrivial consequences and cannot circumvent thermodynamics: cold-to-hot heat transfer may spontaneously occur without an energetic penalty, either cyclically (with entropy barriers) or continuously (with an energy barrier). As the system obeys the first law of thermodynamics, the second law of thermodynamics cannot be applied.

An ideal gas becomes a Knudsen gas when the Knudsen number ($K_n \triangleq \lambda_F / \widehat{D}$) is larger than 1, where λ_F is the mean free path of the gas particles, and \widehat{D} is the characteristic size of the gas container. It has been well known that inherently, a Knudsen gas may not reach thermodynamic equilibrium [1,2]. For instance, when it is immersed in a thermal bath, without extensive particle-particle collision, the fast gas particles tend to frequently collide with the container wall and release heat, while the slow gas particles tend to stay long in the interior. As a result, at steady state, the gas-phase kinetic temperature ($T \triangleq \frac{2}{3} \frac{\bar{K}}{k_B}$) is lower than the container-wall temperature (T_0), where \bar{K} is the average particle kinetic energy, and k_B is the Boltzmann constant; a detailed analysis is given in Note 1 in the Supplemental Material (SM). Moreover, a Knudsen gas may not follow continuum fluid dynamics (e.g., the Knudsen paradox [3]) and could have unique thermal properties (e.g., the Knudsen effect [4]). In mesoscopic physics, somewhat similar nonequilibrium phenomena are also observed, such as the ballistic transport of charge carriers [6].

On the one hand, while the kinetic temperature of a Knudsen gas (T) can be defined by \bar{K} , it is not directly measurable. If we use a temperature sensor, the measurement result at the sensor-

gas interface would be the container-wall temperature (T_0), compatible with the zeroth law of thermodynamics. Knudsen gases are often studied by kinetic theory, not by thermodynamics.

On the other hand, as $T < T_0$, the steady-state internal energy of a Knudsen gas (U) is lower than its equilibrium counterpart (U_0). Notice that thermodynamic equilibrium is an accessible state. If a Knudsen gas is initially at the equilibrium state (at T_0), as it evolves to the nonequilibrium steady state (at T), in accordance with the first law of thermodynamics, the reduction in U must be counterbalanced by a heat desorption (Q). It raises an important question: is this process consistent with the second law of thermodynamics?

Such a concern is reinforced by the fact that the classic H-theorem [7] is inapplicable to Knudsen gas, since the assumption of molecular chaos is irrelevant. That is, there is no kinetic mechanism to maximize entropy. Recently, we investigated the concept of spontaneously nonequilibrium dimension (SND) and showed that, indeed, with locally nonchaotic components, there are macroscopic systems beyond the boundary of the second law of thermodynamics [8,9].

Figure 1(a) depicts the Monte Carlo (MC) simulation of a two-dimensional (2D) gas in a square container. The computer programs are available at [10]; the algorithm is introduced in Note 2 in SM. The gas particles are elastic hard disks, with no long-range force among them. Particle collision is computed by solving Newton's laws. The system is scalable; an example unit system can be based on Å, fs, g/mol, and K. The container size (\hat{L}) is 200; the particle number (N) is 500; the particle diameter (d) is 2; the particle mass (m) is 1; the timestep is 1. The particle mean free path is $\lambda_F = (\hat{L} - d)^2 / (\sqrt{8}Nd) \approx 13.86$, much less than \hat{L} . All the boundaries are thermal walls at constant $T_0 = 100$. When a particle collides with a wall, the reflected direction is random; the reflected speed is not correlated with the incident speed, but randomly follow the 2D Maxwell-Boltzmann distribution $p(v) = \beta_0 m v \cdot e^{-\beta_0 m v^2 / 2}$, where v is the particle speed, and $\beta_0 = 1/(k_B T_0)$. We tested various boundary conditions; they do not affect the main conclusion (see Note 3 in SM).

After the settlement period (2×10^4 timesteps), at each timestep, we calculate the internal energy (U) as the total kinetic energy of all the particles, and the heat desorption (Q) as the accumulated ΔK of all the particle-wall collisions, where $\Delta K = K_i - K_r$, and K_i and K_r are the incident and reflected particle kinetic energies, respectively. At the steady state, a set of divider walls are inserted, evenly separating the large container into 400 small cells (Figure 1b). The cell

size ($\widehat{D} = 10$) is less than λ_F , so that each cell is a Knudsen gas. The inner cell walls use the same boundary condition as the outer walls. The simulation of particle movement continues. At the new steady state, the cell walls are removed, and the simulation keeps running. After the system returns to the initial steady state, a second cycle of cell-wall insertion and removal is operated.

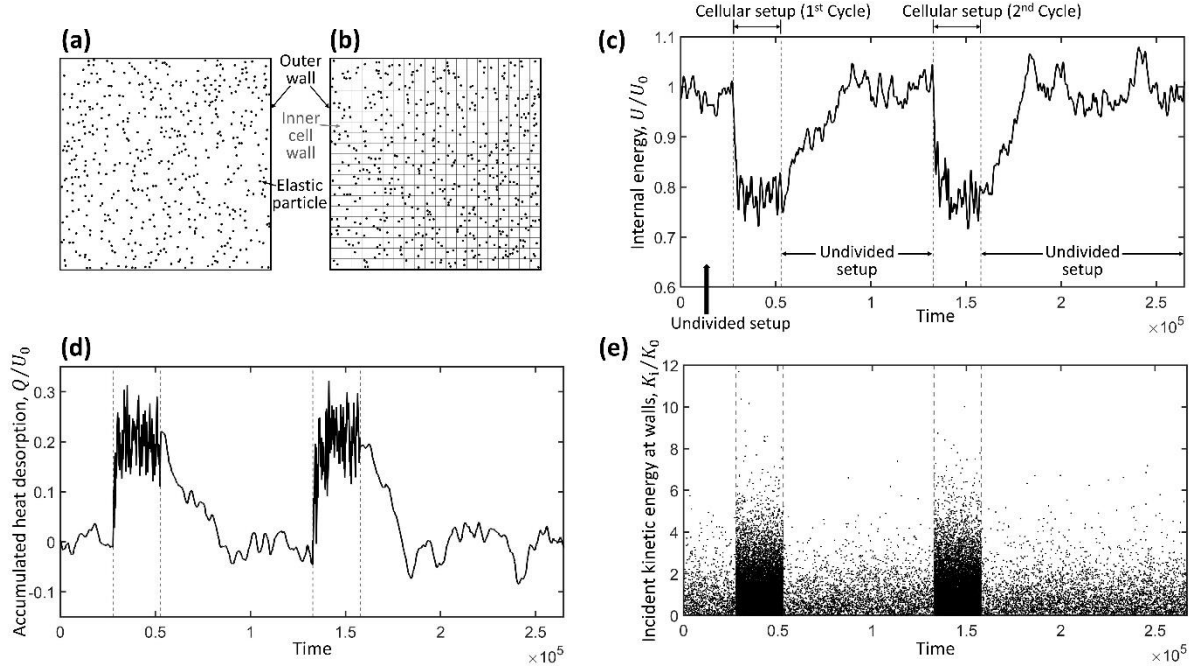


Fig. 1 The first model: **(a)** the undivided setup (a 2D chaotic ideal gas), and **(b)** the cellular setup (each cell is a Knudsen gas). All the outer and inner boundaries are thermal walls at constant temperature T_0 . As the system shifts between the two configurations through cell-wall insertion/removal, the internal energy changes, causing a significant heat flux through the walls. **(c)** A typical time profile of the internal energy (U), in two cycles of cell-wall insertion/removal ($U_0 = 0.029$). For each cycle, the first dashed vertical line indicates cell-wall insertion, and the second dashed vertical line indicates cell-wall removal. **(d)** The accumulated heat desorption across all the walls (Q), reported for every 100 particle-wall collisions. **(e)** The incident particle kinetic energy (K_i) at the container/cell walls; each data point represents a particle-wall collision ($K_0 = k_B T_0$).

Figure 1(c) shows typical running average of U for every 1000 timesteps. When the system is changed from Figure 1(a) to Figure 1(b), the steady-state U decreases by about 20%, agreeing with the literature data [11,12]. Correspondingly, about $0.2U_0$ heat is released from the gas phase into the thermal walls (Figure 1d). Figure 1(e) shows the incident particle kinetic energy (K_i). In the cellular setup, compared to the undivided setup, high-energy particle-wall collisions happen more frequently, as a faster particle has a higher probability to encounter a wall. Consequently, the average K_i is greater than $k_B T$, so that at steady state, although $T < T_0$, the gas-wall heat exchange

is balanced. After the inner walls are removed, the system is shifted back to the undivided state, and absorbs $\sim 0.2U_0$ heat from the environment (Figure 1d). As the cell-wall insertion/removal is repeated, the heat desorption/absorption continues cyclically.

The critical thermal process in Figure 1 occurs at the interface between the nonchaotic phase (the cells) and the chaotic phase (the thermal walls). In the interior of a nonchaotic medium, the heat transport mechanisms are also highly interesting [e.g., 13-16]. Below, we use another model (Figure 2) to demonstrate that in a gravitational field, even without the divider walls, remarkable phenomena may still take place.

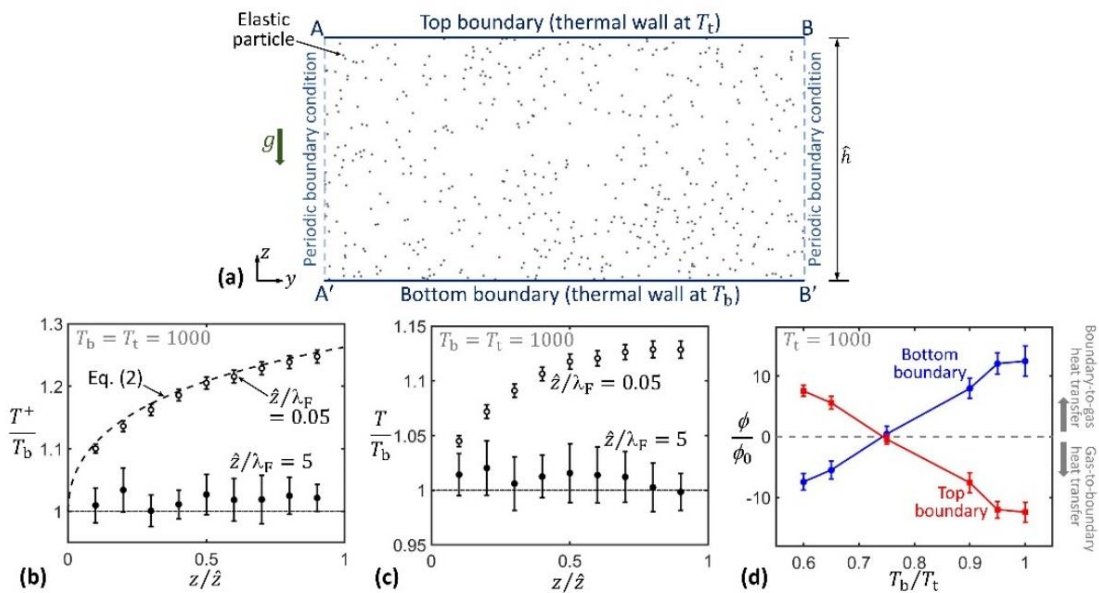


Figure 2 The second model: (a) a 2D gas in a vertical plane in a uniform gravitational field (g). When the plane height (\hat{z}) is less than the nominal particle mean free path (λ_F), it is a Knudsen gas, and the distribution of kinetic temperature cannot reach thermodynamic equilibrium. (b) Typical steady-state distribution of the kinetic temperature (T^+) along height z , for the ascending particles. The dashed curve is calculated from Equation (2). (c) Typical steady-state distribution of the kinetic temperature for all the particles (T). (d) Typical steady-state wall-to-gas heat transfer rates (ϕ) at the top boundary and the bottom boundary, as functions of T_b ($T_t = 1000$; $\hat{z}/\lambda_F = 0.05$). The error bars represent the 95%-confidence interval.

Figure 2(a) shows the MC simulation of a number of 2D billiard-like particles randomly moving in a vertical plane in a uniform gravitational field (g). The left and right borders (AA' and BB') are open and use periodic boundary condition. The upper and lower borders (AB and A'B') are thermal walls; each of them represents a large thermal reservoir. The top-wall and bottom-wall temperatures are denoted by T_t and T_b , respectively. The simulation uses a similar algorithm to Figure 1 [10], with the same unit system. The timestep is 0.01; the particle diameter $d = 1$; $m =$

1; $N = 500$. In all the simulation cases, $T_t = 1000$, and the total area of particle movement is $A_0 = \hat{w}\hat{z} = 39268.75$, where $\hat{z} = \hat{D} - d$, and \hat{w} and \hat{D} are the width and the height of the simulation box, respectively. The nominal particle mean free path is $\lambda_F = A_0/(\sqrt{8}Nd) \approx 27.77$. Different simulation cases may have different \hat{z} ; g is adjusted to maintain a constant Boltzmann factor at the top boundary ($z = \hat{z}$): $\delta_0 = e^{-\beta mg\hat{z}} = 0.607$, where $\beta = 1/(k_B T_b)$. Initially, the particles are randomly distributed in the plane; their speed follows the 2D Maxwell-Boltzmann distribution at T_b , and their direction is random. When $\hat{z} \gg \lambda_F$, the system represents a chaotic ideal gas. When $\hat{z} \ll \lambda_F$, it is a Knudsen gas; as particle-particle collision is negligible, the system performance is dominated by the particle-wall collisions.

The bottom-wall temperature (T_b) is set to be the same as T_t . After the settlement period (10^5 timesteps), we monitor the particle velocity for two simulation cases: $\hat{z}/\lambda_F = 0.05$ and $\hat{z}/\lambda_F = 5$. Along the vertical direction, the plane is virtually divided into 10 equal horizontal layers. Figure 2(b) shows typical steady-state profiles of the kinetic temperature of ascending particles, $T^+ \triangleq \bar{K}_i^+/k_B$, where \bar{K}_i^+ is the average kinetic energy of the particles moving upwards across the lower border of the i -th layer (from bottom to top, $i = 1, 2 \dots 10$). If we consider both the ascending and descending particles, the overall gas-phase temperature is given in Figure 2(c): $T \triangleq \bar{K}_i/k_B$, where \bar{K}_i is the average kinetic energy of all the particles crossing the lower border of the i -th layer.

Maxwell has studied thermal equilibrium of a column of chaotic gas in gravity and concluded [17]: "...the temperature would be the same throughout (i.e., isothermal), or, in other words, gravity produces no effect in making the bottom of the column hotter or colder than the top." This is visualized in Figure 2(b,c): when $\hat{z}/\lambda_F = 5$, both T^+ and T are nearly homogeneous along z . It is consistent with Figure A1 in SM, where the particle flux distribution (\tilde{N}_i) for $\hat{z}/\lambda_F = 5$ follows the Boltzmann factor. Figure A2 in SM shows the reference tests on "ghost" particles. When the particle-particle collision is turned off, regardless of \hat{z}/λ_F , the steady-state distributions of \tilde{N}_i and T^+ are nonequilibrium, indicating that particle interaction is the key factor.

When $\hat{z}/\lambda_F = 0.05$, remarkably, the steady-state distributions of T^+ and T are nonuniform, suggesting that without extensive particle-particle collision, there is no mechanism to drive the system to reach thermal equilibrium (also see the non-Boltzmann distribution of \tilde{N}_i for $\hat{z}/\lambda_F = 0.05$ in Figure A1 in SM). It is counterintuitive that T^+ and T are larger at a higher z , since for every ascending or descending particle, the speed is higher at the bottom. This

phenomenon should be attributed to the fact that, while the high-energy particles may reach the top, many more low-energy particles can only move around the bottom. Overall, the average speed of the particles near the bottom is lower than near the top. The average kinetic energy of the ascending particles can be estimated as

$$\bar{K}^+(z) = \frac{\int_{mgz}^{\infty} (K_z - mgz) \cdot p_z(K_z) dK_z}{\int_{mgz}^{\infty} p_z(K_z) dK_z} + \bar{K}_y \quad (1)$$

where $p_z = e^{-\beta K_z} / \sqrt{\pi K_z k_B T_b}$ is the one-dimensional Maxwell-Boltzmann distribution of the z -dimension kinetic energy (K_z) at the bottom boundary ($z = 0$), and $\bar{K}_y = k_B T_b / 2$ is the average kinetic energy in the horizontal direction. Thus,

$$T^+(z) \triangleq \frac{\bar{K}^+}{k_B} = \left[\frac{\Gamma(3/2, \beta mgz)}{\Gamma(1/2, \beta mgz)} - \frac{mgz}{k_B T_b} + \frac{1}{2} \right] T_b \quad (2)$$

where $\Gamma(x_1, x_2) = \int_{x_2}^{\infty} \tau^{x_1-1} e^{-\tau} d\tau$ is the upper incomplete gamma function. In Figure 2(c), the gradient of T is approximately a half of that of T^+ , which looks plausible, because T accounts for the descending particles, while T^+ does not. The result of T is in agreement with the previous simulation of a two-shelf system [9] (Note 4 in SM). We tested various boundary conditions (see Figure A3 in SM); as long as $\hat{z}/\lambda_F \ll 1$, T always increases with z .

In Figure 2(d), for $\hat{z}/\lambda_F = 0.05$, the average steady-state wall-to-gas heat-transfer rate is calculated as $\phi = \frac{1}{\Delta t} \Sigma(K_r - K_i)$, where Σ indicates summation for all the particles reflected by AB or A'B' during every $\Delta t = 2 \times 10^4$ timesteps. The reference rate is $\phi_0 = k_B T_t / t_0$, with $t_0 = \hat{z} \sqrt{m / (2k_B T_t)}$. For different simulation cases, T_b/T_t is varied from 0.6 to 1.0. Figure A4 in SM shows typical time profiles of ϕ . When $T_b/T_t = 1$, the calculation reflects the nonequilibrium case in Figure 2(b,c). The heat influx at the top wall is dominated by T^+ . As T^+ increases with z , the top wall absorbs heat from the incident particles. The ‘‘extra’’ thermal energy comes from the heat desorbed by the bottom wall. When $T_b/T_t = 0.9$ or $T_b/T_t = 0.95$, the positive $T^+ - z$ gradient overcomes the negative $T_b - T_t$ difference, causing a continuous heat transport from the cold side (the bottom wall at T_b) to the hot side (the top wall at T_t). Only when T_b is much lower than T_t ($T_b/T_t < 0.75$), can hot-to-cold heat transfer occur across the gas phase.

Figure 1(a) represents an ideal gas. It is a typical thermodynamic system and all its behaviors, including the inner walls, should be in line with thermodynamic analysis. The cell walls block the particle movement and influence the probability of particle-particle collision, and thus,

may be viewed as entropy barriers. They are not Maxwell’s demon. No detailed information of microstate is involved. The operation of the cell walls can be pre-programmed, regardless of the specific locations and velocities of individual particles. The generated heat flux is not related to random fluctuation or any irreversible processes (e.g., the nonequilibrium paths associated with the Jarzynski equality [18]). In the cellular setup, the heat desorption spontaneously occurs from the “colder” gas phase (at T) to the “hotter” walls (at T_0). No matter how to define temperature, the heat exchange can be substantial (see Figure A6 in SM) and drive a thermoelectric device to produce useful work by absorbing heat from the environment without any other effect, incompatible with the heat-engine statement of the second law of thermodynamics.

The nonequilibrium steady state, although counterintuitive, follows the principle of maximum entropy [8]. For a canonical ensemble of an equilibrium system, entropy $S \triangleq -k_B \sum_i \rho_i \ln \rho_i$ is maximized to the global maximum (S_{eq}) under the constraints of $\sum_i \rho_i = 1$ and $\sum_i \rho_i \epsilon_i = U$, where ρ_i and ϵ_i are the probability and the energy of the i -th microstate, respectively. The maximization of S is expressed as $\frac{\partial \mathcal{L}_0}{\partial \rho_i} = 0$, where the Lagrangian is $\mathcal{L}_0 = -\sum_i \rho_i \ln \rho_i + \hat{\alpha}(1 - \sum_i \rho_i) + \hat{\beta}(U - \sum_i \rho_i \epsilon_i)$, and $\hat{\alpha}$ and $\hat{\beta}$ are the Lagrange multipliers. Its solution is $\rho_i \propto e^{-\hat{\beta}\epsilon_i}$. In Figure 1(b), the nonchaotic particle movement imposes additional constraints $\rho_i \approx \mu \prod_{k=1}^N t_k$, where $t_k \triangleq \bar{x}_k/v_k$, \bar{x}_k , and v_k are the retention time, the traveling distance, and the speed of the k -th particle, respectively; μ is the normalization factor. The Lagrangian should be redefined as $\mathcal{L}_1 = \mathcal{L}_0 + \sum_i \tilde{\alpha}_i(\mu \prod_{k=1}^N t_k - \rho_i)$, where $\tilde{\alpha}_i$ are the additional Lagrange multipliers. From $\frac{\partial \mathcal{L}_1}{\partial \rho_i} = 0$, we have $\rho_i \propto e^{\tilde{\alpha}_i} e^{-\hat{\beta}\epsilon_i}$, which not only is non-Boltzmannian but also does not satisfy the assumption of equal *a priori* equilibrium probabilities. The more constrained maximization based on \mathcal{L}_1 results in the nonequilibrium entropy (S_{ne}), smaller than the less constrained equilibrium maximum S_{eq} . The second law of thermodynamics may be generalized as follows [9]: in an isolated system, entropy (S) always evolves toward the maximum possible steady-state value (S_Q), i.e., $S \rightarrow S_Q$. For a chaotic system, $S_Q = S_{\text{eq}}$, so that $S \rightarrow S_Q$ is equivalent to the classical entropy statement of the second law of thermodynamics. For a nonchaotic system, $S_Q = S_{\text{ne}}$. If initially $S > S_Q$, entropy could decrease.

In Figure 2, the spontaneous cold-to-hot heat transfer is not subject to any energetic penalty, contradicting the refrigeration statement of the second law. Moreover, because the gradient of T

is dependent on the gravitational energy barrier ($mg\hat{z}$), two different gases can form Maxwell's double-column engine [19] that continuously produces work by absorbing heat from the environment (Note 5 and Figure A5 in SM). There are a few points worth noting. Firstly, in Figure 2(d), the heat desorption of gas at the upper boundary is balanced by the heat absorption at the lower boundary, obeying the first law of thermodynamics. Secondly, the system does not consume energy from the gravitational field. At steady state, on average, for every ascending particle, there is a descending particle; vice versa. Thirdly, Figure 2(a) is fundamentally different from Earth's atmosphere [20] (Note 6 in SM).

In the weak gravitational field of Earth ($\beta mg\hat{z} \approx 10^{-12}$ for air molecules), the nonequilibrium phenomena in Figure 2(b-d) are negligible. It would be interesting to explore whether in high- g environments the nonchaoticity effects could be nontrivial, and whether the concept might be demonstrated by using a stronger thermodynamic force, such as Coulomb force. Notice that if we place a metallic nanolayer in an electric field, the screening effect must be taken into consideration.

Figure 1 circumvents the hurdle of high energy barrier. However, in reality, the idealized process of cell-wall insertion/removal may be difficult to achieve, because gas transport in nanochannels is influenced by surface adsorption and desorption [e.g., 21]. Interestingly, in a study on nonwetting liquids in nanopores, there may have already been experimental evidence [22,23]: associated with liquid defiltration from a hydrophobic nanoporous silica, temperature significantly decreases (see Note 7 and Figure A6 in SM). Figure A7 in SM illustrates an equivalent design of circular flow, in which the particle adsorption and desorption are balanced at steady state. The resistance to the movement of the nonwetting liquid tends to be low, thanks to the Knudsen paradox [3,4] and the superfluidity effect [24-26] in nanoenvironments. Multiple setups may be arranged in parallel or in tandem, to amplify the temperature difference and the heat flux. If the concept is applied to the charge carriers in a mesoscopic physical system, entropy barriers (i.e., the "cell walls") may be realized through asymmetric scattering or reflection with variable probability/energy/angle, and the upper limit of the power density might be on the scale of 10^4 kW/mm³ (Note 8 in SM).

In summary, people are well aware that certain nonchaotic particle movements cannot be analyzed by thermodynamics [27,28]; usually, such phenomena only happen on small scales, and their energy properties are "trivial". In current research, we show that, beyond the boundary of the

second law of thermodynamics, there are also macroscopic systems, and the consequences are nontrivial. One example is the switchable structure of the Knudsen-gas cells (Figure 1); another example is the Knudsen gas in gravity (Figure 2). In both cases, heat can spontaneously transfer from the cold side to the hot side, without an energetic penalty.

References

1. S. R. De Groot, P. Mazur. *Non-Equilibrium Thermodynamics*. Courier Corporation (2013)
2. James Jeans. *An Introduction to the Kinetic Theory of Gases*. Cambridge Univ. Press (1982)
3. M. N. Kogan. *Rarefied Gas Dynamics*. New York: Springer (1969).
4. A. S. Kannan, T. S. B. Narahari, Y. Bharadhwaj, A. Mark, G. Sardina, D. Maggiolo, S. Sasic, H. Ström. The Knudsen paradox in micro-channel Poiseuille flows with a symmetric particle. *Appl. Sci.*, **11**, 351 (2021)
5. Z. Ulker, D. Sanli, C. Erkey. Applications of aerogels and their composites in energy-related technologies. In: V. Anikeev, M. Fan (ed.), *Supercritical Fluid Technology for Energy and Environmental Applications*, Elsevier (2014).
6. A. Kawabata. Ballistic electron transport. In: T. Ando, Y. Arakawa, K. Furuya, S. Komiyama, H. Nakashima (ed.), *Mesoscopic physics and electronics* (Springer, 1998)
7. M. Kardar. *Statistical Physics of Particles* (Cambridge Univ. Press, 2007), p. 74.
8. Qiao Y, Shang Z. Producing useful work in a cycle by absorbing heat from a single thermal reservoir: An investigation on a locally nonchaotic energy barrier. *Physica A* **596**, 127105 (2022)
9. Y. Qiao, Z. Shang, R. Kou. Molecular-sized outward-swinging gate: Experiment and theoretical analysis of a locally nonchaotic barrier. *Phys. Rev. E* **104**, 064133 (2021)
10. See Supplemental Material for the computer programs used in the current research, which are also available at http://mmrl.ucsd.edu/Z_Upload/Papers/SupplMater_KnudsenGas.zip
11. H. J. Kreuzer, R. Teshima. Time evolution and thermalization of an ideal gas in a box. *Can. J. Phys.* **55**, 189 (1977)
12. T. Mortia, Y. Fukui. Thermalization of the ideal gas in a one-dimensional box. *Can. J. Phys.* **57**, 1103 (1979).
13. S. Lepri, R. Livi, A. Politi. Heat conduction in chains of nonlinear oscillators. *Phys. Rev. Lett.* **78**, 1896 (1997).

14. D. Alonso, A. Ruiz, I. de Vega. Polygonal billiards and transport: diffusion and heat conduction. *Phys. Rev. E* **66**, 066131 (2002).
15. R. Livi, S. Lepri. Heat in one dimension. *Nature* **421**, 327 (2003).
16. B. Li, G. Casati, J. Wang, T. Prosen. Fourier law in the alternate-mass hard-core potential chain. *Phys. Rev. Lett.* **92**, 254301 (2004).
17. J. C. Maxwell. *Theory of Heat* (Longmans, Green, and Co., London, 1872), p. 300
18. C. Jarzynski. Nonequilibrium equality for free energy differences. *Phys. Rev. Lett.* **78**, 2690 (1997).
19. J. C. Maxwell. On the dynamical theory of gases. *London Edinburgh Dublin Phil. Mag. J. Sci.* **35**, 215, 1868
20. J. C. Maxwell. The dynamic evidence of the molecular constitution of bodies. In: W. D. Niven (ed.), *The Scientific Papers of James Clerk Maxwell Vol. 2* (Cambridge Univ. Press, 2010) p. 434.
21. T Wu, D Zhang. Impact of adsorption on gas transport in nanopores. *Scientific Reports* **6**, 23629 (2016)
22. A. Han, V. K. Punyamurtula, Y. Qiao. Heat generation associated with pressure-induced infiltration in a nanoporous silica gel. *J. Mater. Res.* **23**, 1902 (2008).
23. A. Han, W. Lu, V. K. Punyamurtula, T. Kim, Y. Qiao. Temperature variation in liquid infiltration and defiltration in a MCM41. *J. Appl. Phys.* **105**, 024309 (2009).
24. B. J. Hinds, N. Chopra, T. Rantell, R. Andrews, V. Ravalas, L. G. Bachas. Aligned multiwalled carbon nanotube membranes. *Science* **303**, 62 (2004).
25. A. A. Gusev, O. Guseva. Rapid mass transport in mixed matrix nanotube/polymer membranes. *Adv. Mater.* **19**, 2672 (2007).
26. Han A, Lu W, Punyamurtula VK, Chen X, Surani FB, Kim T, Qiao Y. Effective viscosity of glycerin in a nanoporous silica gel. *J. Appl. Phys.* **104**, 124908 (2008).
27. G. Lebon, D. Jou. *Understanding Nonequilibrium Thermodynamics* (Springer, 2008)
28. J. R. Dorfman. *An Introduction to Chaos in Nonequilibrium Statistical Mechanics* (Cambridge University Press, Cambridge, 1999).

Supplemental Material

for

Spontaneous cold-to-hot heat transfer in Knudsen gas

Yu Qiao^{1,2,*}, Zhaoru Shang¹

¹ Program of Materials Science and Engineering, University of California – San Diego, La Jolla, CA 92093, U.S.A.

² Department of Structural Engineering, University of California – San Diego, La Jolla, CA 92093-0085, U.S.A.

* Corresponding author (email: yqiao@ucsd.edu)

The computer programs used in the current investigation can be downloaded from [URL]. They are also available at http://mmrl.ucsd.edu/Z_Upload/Papers/SupplMater_KnudsenGas.zip

Note 1. Consider the steady state of a Knudsen gas in a specular-wall container ($K_n > 1$). Assume that the particle-particle collision is negligible, and the particle speed (v) follows the Maxwell-Boltzmann distribution. During time \bar{t}_0 , the number of particle-wall collisions per unit area may be written as $\bar{N}_c = \rho_0 \bar{t}_0 \cdot \frac{1}{2} \int_0^\infty [v_x \cdot p_x(v_x)] dv_x$, where ρ_0 is the particle number density, v_x is the component of particle velocity normal to the boundary, $p_x = \sqrt{2\beta m/\pi} e^{-\beta m v_x^2/2}$ is the one-dimensional Maxwell-Boltzmann distribution function of $|v_x|$, m is the particle mass, $\beta = 1/(k_B T)$, k_B is the Boltzmann constant, and T is the gas-phase kinetic temperature. The container-wall temperature is determined by the average kinetic energy of the incident particles that collide with the walls:

$$T_0 = \frac{1}{k_B} \left[\frac{\rho_0 \bar{t}_0 \cdot \frac{1}{2} \int_0^\infty \frac{mv_x^2}{2} [v_x \cdot p_x(v_x)] dv_x}{\bar{N}_c} + (\mu - 1) \frac{k_B T}{2} \right] = \bar{\mu} \cdot T,$$

where μ is the number of dimensions of the system, and $\bar{\mu} = (\mu + 1)/\mu$; the term of $(\mu - 1)k_B T/2$ is the average particle kinetic energy in the dimension(s) parallel to the boundary. For a two-dimensional Knudsen gas, $\bar{\mu} = 3/2$; for a three-dimensional Knudsen gas, $\bar{\mu} = 4/3$. In comparison, in a chaotic gas, no particle can reach the boundary without being interrupted by other particles, and the influx at the boundary should be calculated through the mean-field theory: $\bar{N}'_c = \rho_0 (\bar{v}_x \bar{t}_0)/2$, with \bar{v}_x being the average v_x . Thus, $T_0 = \frac{2}{k_B \mu} \left[\bar{N}'_c \cdot \int_0^\infty \frac{mv^2}{2} p(v) dv \right] / \bar{N}'_c = T$, i.e., thermal equilibrium is reached.

Notice that if the container of the Knudsen gas is formed by thermal walls (e.g., Figure 1b in the main text), the probability density of particle speed would be non-Boltzmannian and therefore, the above analysis of $T_0 = \bar{\mu} \cdot T$ is no longer applicable. In fact, under this condition, the particle-particle interaction cannot be entirely ignored. Otherwise, the slowest gas particles tend to remain in the interior, as the fast particles randomly change velocities upon particle-wall collisions. With a constant T_0 , because $\int_0^\infty v_x^{-1} p_x dv_x \rightarrow \infty$, the calculated gas-phase kinetic temperature (T) would be unrealistically low. In current research, we rely on the Monte Carlo simulation to quantitatively investigate the system performance.

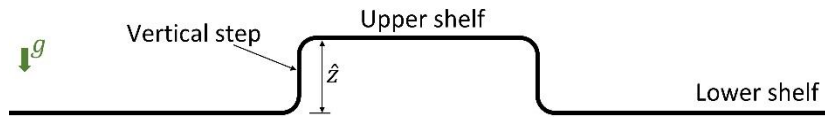
Note 2. In the 2D system, the particles are finite-sized hard disks. The particle-particle and particle-wall collisions happen in the middle of the timesteps. In each timestep, the program first computes

the virtual position of every particle at the end of the timestep, as if particle collision could not occur. Then, collision is identified as the particle-particle or particle-wall overlapping. The exact collision location and time are calculated by tracing the particle trajectories, and the correct particle information is updated by solving Newton's equations (conservation of energy and momentum). Finally, the next timestep begins. The time resolution is high, so that the expected value of the particle displacement in a timestep is less than 5% of the particle size; the probability of missing a collision is practically zero (less than 10^{-170}).

The cell-wall insertion or removal does not take time. During cell-wall insertion, if a particle overlaps with a cell wall, the particle would be moved away from the wall by one particle radius, with everything else being unchanged. If this leads to further conflict with another particle, the simulation case would be abandoned.

Note 3. In a set of numerical experiments, we tested different boundary conditions. When a particle collides with a wall, the reflected direction is random, and the reflected speed is $v_{re} = \tilde{\alpha}v_{in} + (1 - \tilde{\alpha})v_{rand}$, where v_{in} is the incident speed, v_{rand} is a speed randomly generated from the 2D Maxwell-Boltzmann distribution at T_0 , and $\tilde{\alpha}$ represents the “memory” of the particle-wall collision. In different simulations, $\tilde{\alpha}$ is varied from 0 to 1/2. When $\tilde{\alpha} = 0$, v_{re} is reduced to the ideal thermal-wall condition in the main text; when $\tilde{\alpha} > 0$, the degree of randomness of the particle-wall collision is lower. The simulation results confirmed that in the range of $\tilde{\alpha}$ under investigation, its value does not have a significant influence on the steady state.

Note 4. In [9], a Monte Carlo simulation was performed on a two-shelf system, as depicted in the diagram on the right.



Two shelves are at different heights in a uniform gravitational field (g), connected through a vertical step. A large number of two-dimensional elastic particles (hard disks) randomly move on the two shelves across the vertical step. The shelf size is large, so that the particle movement in the shelves is ergodic and chaotic. The height difference (\hat{z}) between the two shelves is much less than the nominal particle mean free path (λ_F), so that the particle transmission across the step tends to be locally nonchaotic. Compared to Figure 2(a) in the main text, the step is analogous to the vertical plane, and the chaotic gases in the two shelves are the counterparts of the thermal walls.

When $\beta mg\hat{z} = 0.5$, it was observed that at steady state, the average particle speed on the upper shelf was larger than on the lower shelf by $10.4 \pm 1.3\%$, where β is the thermodynamic beta and m is the particle mass; the data range indicates the 90%-confidence interval. The average particle number density ratio between the upper shelf and the lower shelf is significantly less than the Boltzmann factor $e^{-\beta mg\hat{z}}$, consistent with the lower curve in Figure A1 below.

Note 5. In [19], for thermal equilibrium in gravity, Maxwell pointed out: “...if the temperature of any substance, when in thermic equilibrium, is a function of the height, that of any other substance must be the same function of the height. For if not, let equal columns of the two substances be enclosed in cylinders impermeable to heat, and put in thermal communication at the bottom. If, when in thermal equilibrium, the tops of the two columns are at different temperatures, an engine might be worked by taking heat from the hotter and giving it up to the cooler, and the refuse heat would circulate round the system till it was all converted into mechanical energy, which is a contradiction to the second law of thermodynamics. The result as now given is, that temperature

in gases, when in thermal equilibrium, is independent of height, and it follows from what has been said that temperature is independent of height in all other substances.”

Note 6. In [20], Maxwell stated: “In the case of the atmosphere, the effect of wind is to cause the temperature to vary as that of a mass of air would do if it were carried vertically upwards, expanding and cooling as it ascends.”

Earth’s atmosphere is exposed to the ground and outer space, resulting in the macroscopic vertical convection of air. As air rises, it undergoes adiabatic expansion and tends to be colder at the top. On the contrary, in Figure 2(a) in the main text, when $T_b = T_t$, the system is closed and immersed in a thermal bath, so that there is no convection. Even if gas could rise, without particle-particle collision, the increase in volume would not do work, like free expansion in vacuum. That is, the Knudsen gas has no mechanism to render the top section cooler. In fact, in Figure 2 in the main text, T is higher at the top.

Note 7. In [22,23], as depicted in Figure A6(a) below, nanoporous particles are immersed in a nonwetting liquid, sealed in a steel container. The particle-to-liquid mass ratio is around 1:5. A pressure (P) is maintained on the liquid phase through the piston, so that the liquid is forced to fill the nanopores. Then, P is gradually reduced, accompanied by liquid defiltration. The temperature of the bulk liquid phase is monitored by the embedded sensor. Figure A6(b) below shows typical measurement data [22]. In an equilibrium system, as the work of P and the effective solid-liquid interfacial tension counterbalance each other, there should not be any temperature variation. If the piston motion were not quasistatic, the effects of viscosity and the out-of-equilibrium liquid molecular movement would have caused a temperature increase, not a temperature decrease. A counterexample of this process is that temperature tends to decrease when water molecules leave a hydrophilic surface (e.g., a water film or a wettable solid surface).

The measured reduction in temperature may be attributed to the “Knudsen gas like” characteristic of the confined liquid: As the nanopore size is somewhat on the same scale as the mean free path of the liquid molecules, the kinetic temperature of the confined liquid is less than that of the environment. Thus, when the confined liquid molecules move out of the nanopores, the temperature of the bulk liquid phase becomes lower. Similarly, associated with the liquid infiltration, a nontrivial temperature increase was observed [22,23].

Note 8. For the sake of simplicity and to be conservative, in a metal, we only consider the high-energy conduction electrons that approximately follow the Maxwell-Boltzmann distribution. Their number density is on the scale of $10^{20}/\text{cm}^3$ and their energy is a few eV, leading to an overall energy density on the scale of 10^7 J/m^3 . In Figure 1(d) in the main text, the heat desorption is ~20% of the internal energy and the duration of each cycle is ~0.1 ns. If these parameters are also relevant to the charge carriers, the upper limit of the power density may be on the scale of 10^4 kW/mm^3 .

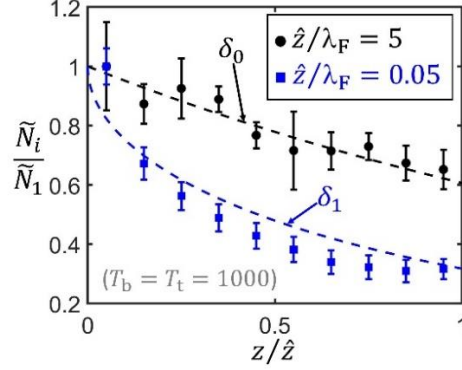


Figure A1. Along the vertical direction (z), the plane in Figure 2(a) in the main text is virtually divided into 10 equal horizontal layers. After the settlement period (10^5 timesteps), we begin to count the particle flux \tilde{N}_i , the number of the particles crossing the lower border of the i -th layer in every 1000 timesteps (from bottom to top, $i = 1, 2 \dots 10$). The normalization factor (\tilde{N}_1) is 56.10 or 103.73 for the equilibrium case ($\hat{z}/\lambda_F = 5$) and the nonequilibrium case ($\hat{z}/\lambda_F = 0.05$), respectively. The error bars represent the 95%-confidence interval. When $\hat{z}/\lambda_F = 5$, with extensive particle-particle collision, \tilde{N}_i fits well with the Boltzmann factor, $\delta_0 = e^{-\beta mgz}$. It reflects the behavior of a chaotic ideal gas. When particle-particle collision is negligible ($\hat{z}/\lambda_F = 0.05$), because the horizontal-dimension particle kinetic energy (K_y) has little contribution to the vertical movement, fewer particles can overcome the gravitational energy barrier. Consequently, \tilde{N}_i is dominated by the z -component of particle velocity (v_z) [9], and it tends to follow $\delta_1 = \int_{\sqrt{2gz}}^{\infty} p_z(v_z) dv_z = 1 - \text{erf}(\sqrt{\beta mgz})$, with $p_z = \sqrt{2\beta m/\pi} e^{-\beta m v_z^2/2}$ being the one-dimensional Maxwell-Boltzmann distribution of v_z . It reflects the behavior of a nonchaotic Knudsen gas.

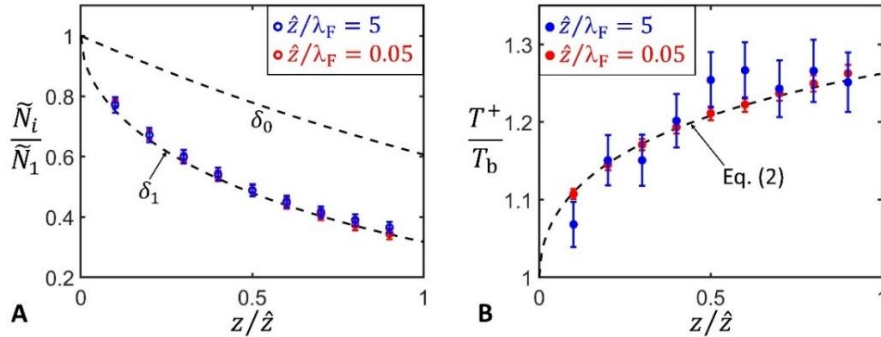


Figure A2. Reference simulation for “ghost” particles. The particle-particle collision is turned off. All the other parameters and procedures are the same as in Figure 2 in the main text ($T_b = T_t = 1000$). The red and the blue data points nearly overlap with each other. **(A)** The steady-state distribution of particle flux (\tilde{N}_i) along height z . The upper dashed curve indicates the Boltzmann factor, $\delta_0 = e^{-\beta mgz}$; the lower dashed curve indicates $\delta_1 = 1 - \text{erf}(\sqrt{\beta mgz})$; \tilde{N}_1 is defined in Figure A1 above. **(B)** The steady-state distribution of the kinetic temperature (T^+) along height z , for the ascending particles. The dashed curve is calculated from Equation (2) in the main text. The error bars represent the 95%-confidence interval.

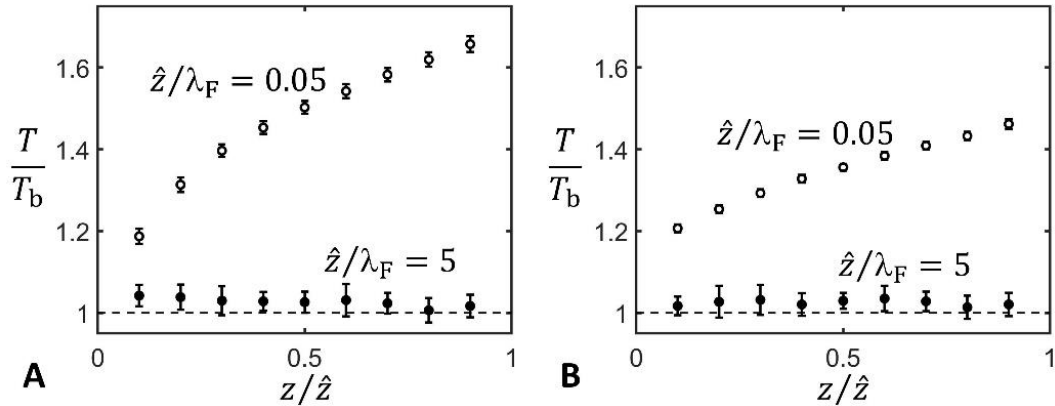


Figure A3. Effects of the boundary condition on the distribution of the gas-phase kinetic temperature (T). **(A)** Both of the bottom and the top boundaries are diffusive walls. The reflected particle direction is random; the reflected particle speed equals to the incident speed. **(B)** The bottom boundary is a thermal wall (the same as in Figure 2 in the main text); the top boundary is a diffusive wall (the same as in panel A). All the other settings and procedures are the same as in Figure 2 in the main text. The error bars represent the 95%-confidence interval.

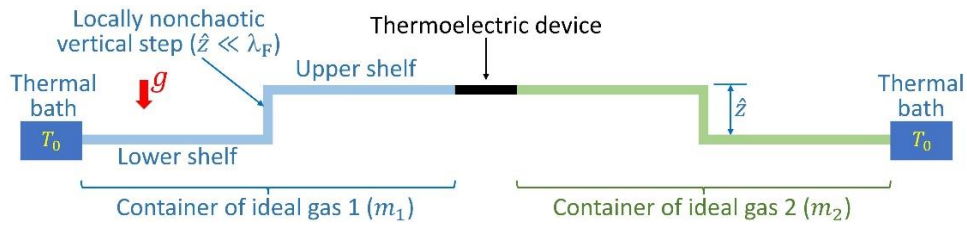


Figure A4. An example of Maxwell's double-column engine [19]. Two identical containers contain different ideal gases, in a uniform gravitational field (g). The gas-particle masses in the two containers are m_1 and m_2 , respectively. Each container has an upper shelf and a lower shelf, with the height difference (\hat{z}) much less than the normal mean free path of the gas particles (λ_F). The lower shelves of the two containers are in contact with the same thermal bath at temperature T_0 . A thermoelectric device is sandwiched in between the two upper shelves. If the temperature field in the container is nonuniform along the vertical direction, because $m_1 \neq m_2$, the effective gas-phase temperatures at the two upper shelves are different. Thus, the thermoelectric device can continuously produce useful work, by absorbing heat from the thermal bath without any other effect.

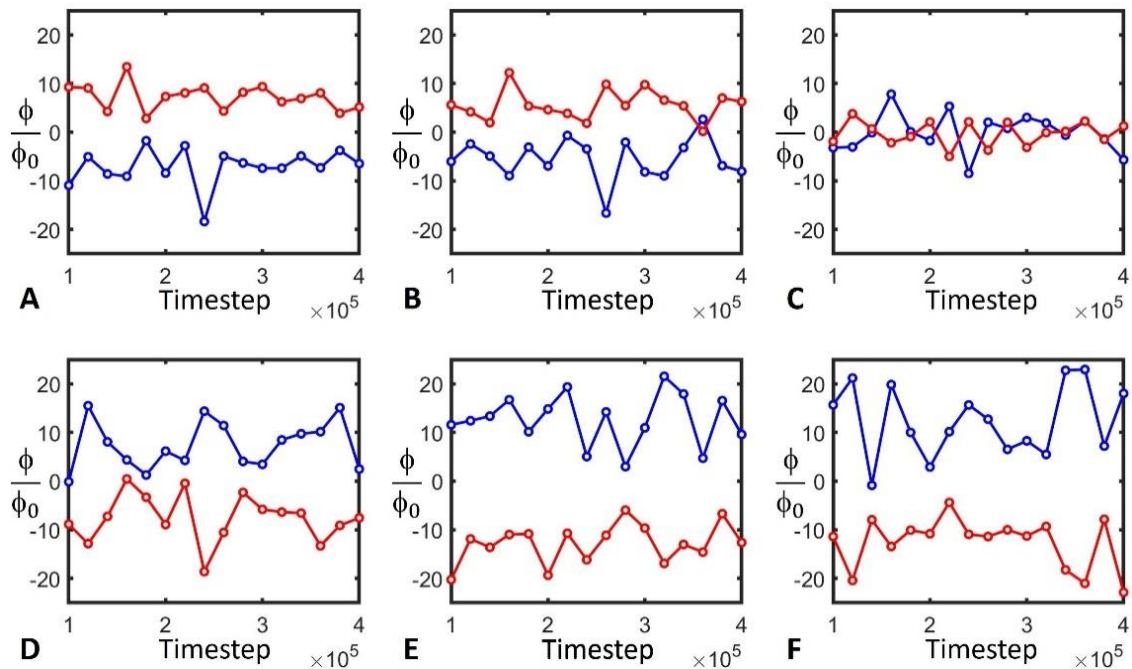


Figure A5. For the system in Figure 2(a) in the main text: typical time profiles of the wall-to-gas heat transfer rates at the top thermal wall (the red lines) and the bottom thermal wall (the blue lines). (A) $T_b = 600$; (B) $T_b = 650$; (C) $T_b = 750$; (D) $T_b = 900$; (E) $T_b = 950$; (F) $T_b = 1000$. In all the simulation cases, $T_t = 1000$. In (A,B), heat transfers from the top wall to the bottom wall across the gas phase; in (D,E,F), heat transfers from the bottom wall to the top wall across the gas phase.

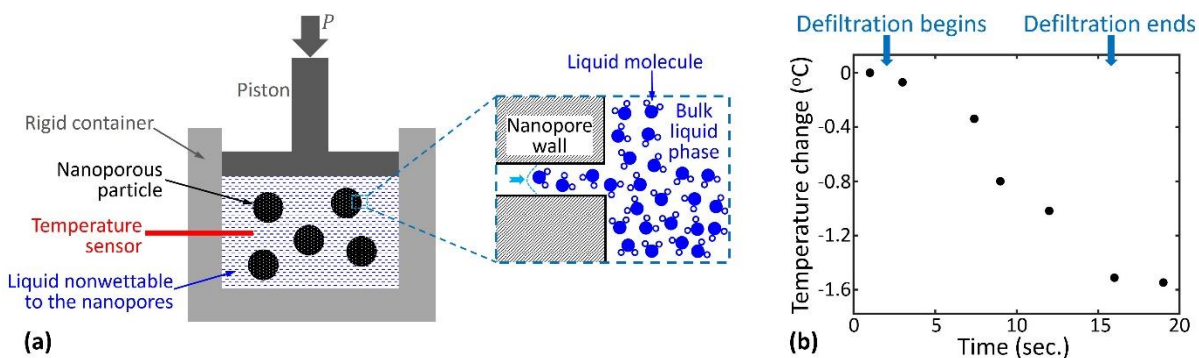


Figure A6. (a) Schematic of the experimental setup in [22,23]. The temperature change associated with the liquid defiltration from the nanoporous particles is measured (see Note 7 above). (b) Typical testing data [22]: temperature considerably decreases when the nonwetting liquid defiltrates out of the nanoporous silica gel, inconsistent with equilibrium thermodynamics (temperature should remain constant or increase).

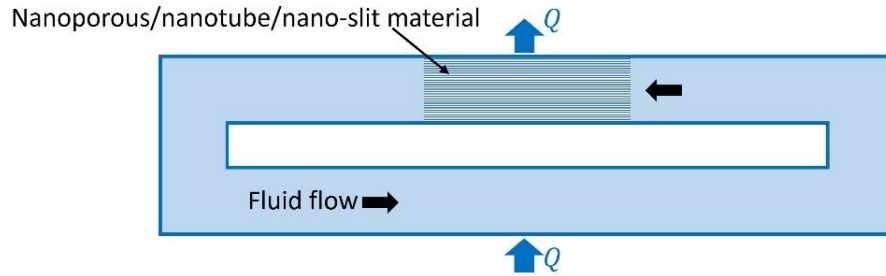


Figure A7 Schematic of a nanofluidic setup of continuous flow, based on the same concept as in Figure A6 above. The system is closed and immersed in a thermal bath. The nanochannel size is smaller than or comparable with the mean free path of the fluid particles. At the steady state, the adsorption and desorption processes are balanced at the inner walls of the nanochannels. As the fluid enters the nanochannels, it releases heat (Q) to the environment, due to the nonequilibrium effect. Likewise, when the fluid comes out of the nanochannels, it absorbs heat from the environment. Such a mechanism may lead to spontaneous cold-to-hot heat transfer, which allows for production of useful work by absorbing heat from the thermal bath without any other effect. The resistance to the flow tends to be low, thanks to the Knudsen paradox [3,4] and the superfluidity effect [e.g., 24-26] in nanoenvironments.